REVISTA INTERDISCIPLINAR DE PESQUISA EM ENGENHARIA

CILAMCE 2016
XXXVII IBERIAN LATIN AMERICAN CONGRESS ON COMPUTATIONAL METHODS IN ENGINEERING
BRASÍLIA - DF - BRAZIL

ELASTIC WAVE BAND GAPS IN A TWO-DIMENSIONAL MAGNETOELECTROELASTIC PHONONIC CRYSTAL

Edson Jansen Pedrosa de Miranda Júnior[1,2]

José Maria Campos dos Santos[1]

edson.jansen@ifma.edu.br

zema@fem.unicamp.br

[1]Department of Computational Mechanics, Faculty of Mechanical Engineering, University of Campinas

[1]Mendeleyev Street, 200, Cidade Universitária "Zeferino Vaz", Barão Geraldo, 13083860, Campinas, SP, Brazil

[2]Department of Professional Education, Centro Histórico Campus, Federal Institute of Education, Science and Technology of Maranhão

[2]Afonso Pena Street, 174, Centro, 65010030, São Luís, MA, Brazil

Abstract. *In this study we investigated the band structure of elastic waves propagating in a magnetoelectroelastic phononic crystal (MPC), consisting of a polymer matrix reinforced by $BaTiO_3$–$CoFe_2O_4$ inclusions in a square, triangular and honeycomb lattices. We also studied the influence of the inclusion geometry cross section – circular, hollow circular, square and rotated square with a 45° angle of rotation with respect to the x, y axes. The plane wave expansion (PWE) method was used to solve the constitutive equations of a magnetoelectroelastic material considering the wave propagation in the xy plane (longitudinal-transverse vibration, XY mode, and transverse vibration, Z mode). The complete band gaps between the XY and Z modes were observed to all types of inclusion and the best performance depends on the lattice. For square lattice, the best performance was found for square inclusion in lower frequencies, for triangular lattice, the circular, square and rotated square present, approximately, the same behavior and for honeycomb lattice, the best performance was found for circular inclusion.*

Keywords: *Magnetoelectroelastic phononic crystal, In-plane wave propagation, Full band gaps, Vibration control, Plane wave expansion method.*

1 INTRODUCTION

Artificial periodic composites known as phononic crystals (PCs), consisting of a periodic array of scatterers embedded in a host medium, have been quite studied (Sigalas *et al.*, 1994; Kushwaha *et al.*, 1994; Pennec *et al.*, 2010; Huang *et al.*, 2013; Yu *et al.*, 2013; Anjos *et al.*, 2015; Miranda Jr. *et al.*, 2015; Miranda Jr. *et al.*, 2016a). PCs have received renewed attention because they exhibit complete band gaps where mechanical (elastic or acoustic) wave propagation is forbidden. The physical origin of phononic and photonic band gaps can be understood at micro-scale using the classical wave theory to describe the Bragg and Mie resonances, respectively, based on the scattering of mechanical and electromagnetic waves propagating within the crystal (Olsson III *et al.*, 2009).

PCs can be applied in many situations, such as vibration isolation technology (Jensen, 2003; Wang *et al.*, 2005; Casadei *et al.*, 2012; Miranda Jr. *et al.*, 2016b; Miranda Jr. *et al.*, 2016c), acoustic barriers/filters (Ho *et al.*, 2003; Yang *et al.*, 2003; Qiu *et al.*, 2005), noise suppression devices (Casadei *et al.*, 2010; Xiao *et al.*, 2012) and surface acoustic devices (Benchabane *et al.*, 2006).

Many types of smart PCs, like piezoelectric PCs (Wilm *et al.*, 2001; Wilm *et al.*, 2002; Wilm *et al.*, 2003; Hou *et al.*, 2004; Lian *et al.*, 2016) and piezomagnetic PCs (Robillard *et al.*, 2009; Vasseur *et al.*, 2011; Bou Matar *et al.*, 2012) were studied. However, only recently, few studies focused on magnetoelectroelastic phononic crystals (MPCs) (Wang *et al.*, 2008; Wang *et al.*, 2009).

In this study, we focused on elastic wave propagation in a MPC. We considered the wave propagation in the *xy* plane (longitudinal-transverse vibration, *XY* mode, and transverse vibration, *Z* mode) in an inhomogeneous transversely isotropic elastic solid. The main purpose of this study was to investigate the elastic band structure of $BaTiO_3$–$CoFe_2O_4$/Polymer PC in a square, triangular and honeycomb lattices with different types of inclusion cross sections: circular, hollow circular, square and rotated square with a 45° angle of rotation with respect to the *x*, *y* axes.

2 THE MODEL

Figure 1 (a), (b) and (c) sketch the cross section of the $BaTiO_3$–$CoFe_2O_4$/Polymer PC taking into account square, triangular and honeycomb lattices, respectively, with an arbitrary inclusion geometry. Figure 1 (d), (d) and (e) represent the irreducible Brillouin zone (IBZ) for the square, triangular and honeycomb lattices, respectively. It is important to highlight that exist three variations in the hexagonal lattice: triangular, honeycomb (or graphite) and kagome lattices (Dyogtyev *et al.*, 2010). In this study we considered four types of inclusion as mentioned before: circular, hollow circular, square and rotated square with a 45° angle of rotation with respect to the *x*, *y* axes.

The constitutive equations of a magnetoelectroelastic material are (Wang *et al.*, 1996):

$$\sigma_{ij} = c_{ijkl}u_{k,l} + e_{lij}\phi_{,l} + q_{lij}\varphi_{,l},$$
$$D_i = e_{ikl}u_{k,l} - \epsilon_{il}\phi_{,l} - \lambda_{il}\varphi_{,l},$$
$$B_i = q_{ikl}u_{k,l} - \lambda_{il}\phi_{,l} - \Gamma_{il}\varphi_{,l}, (i,j,k,l = 1,2,3), \quad (1)$$

where σ_{ij} is the elastic stress tensor, D_i is the electric displacement vector, B_i is the magnetic induction, u_i is the elastic displacement vector, ϕ is the electric potential, φ is the magnetic potential, e_{lij} are the piezoelectric coefficients, q_{lij} are the piezomagnetic coefficients, ϵ_{il} are the dielectric coefficients, Γ_{il} is the magnetic permeability, λ_{il} are the electromagnetic constants, c_{ijkl} is the elastic stiffness.

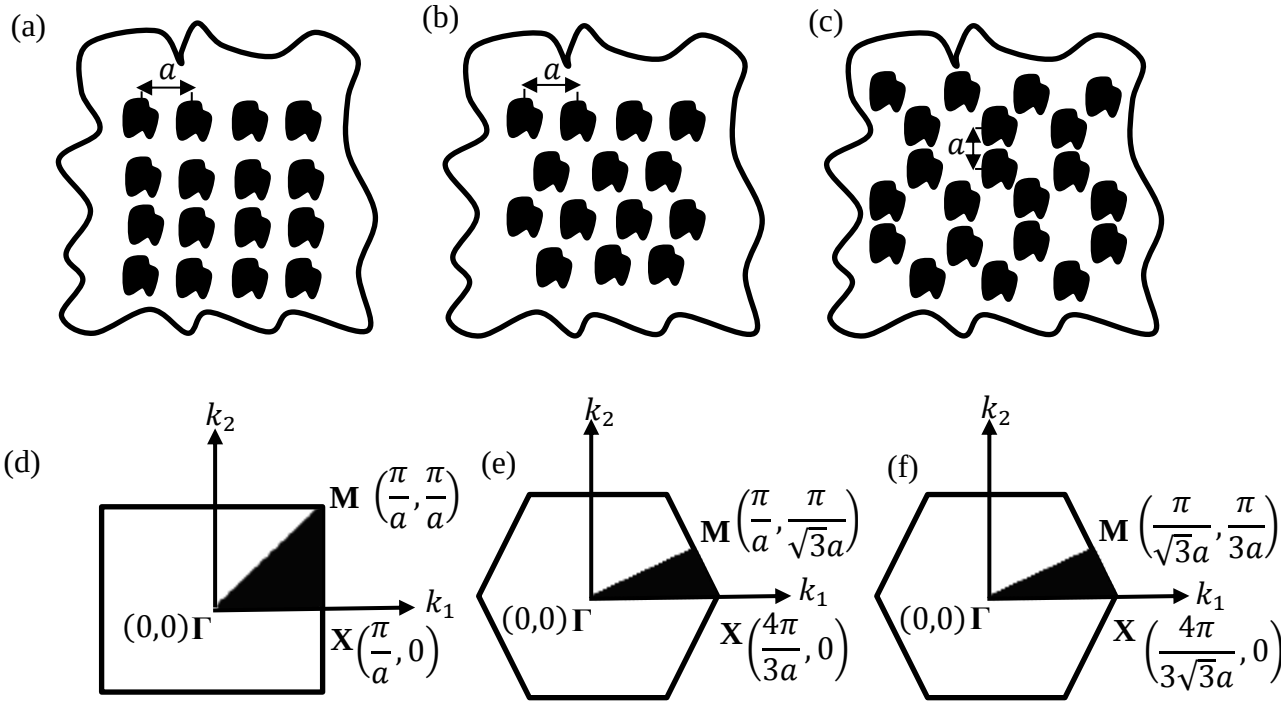

Figure 1. The transverse cross section of the binary composite system: an array of inclusions ($BaTiO_3$–$CoFe_2O_4$) periodically distributed in a matrix (polymer) for square (a), triangular (b) and honeycomb (c) lattices. The IBZ (in shaded region) for square (d), triangular (e) and honeycomb (f) lattices.

We restricted the treatment to linear media, thus the elastic strain tensor ε_{kl} is simplified. Additionally, based on the quasi-static approximation, there are no electromagnetic sources and the curls are zero, thus the electric and magnetic fields are taken as gradients of scalar potentials and one can write:

$$\varepsilon_{kl} = \frac{1}{2}\left(u_{k,l} + u_{l,k}\right),\ \ E_l = -\frac{\partial \phi}{\partial x_l} = \phi_{,l},\ \ H_l = -\frac{\partial \varphi}{\partial x_l} = \varphi_{,l}, \tag{2}$$

where E_l is the electric field and H_l is the magnetic field.

The differential equations of motion in the absence of body forces are given by:

$$\sigma_{ij,i} = \rho \ddot{u}_j, D_{i,i} = 0, B_{i,i} = 0, \tag{3}$$

where ρ is the mass density and dot denotes differentiation with respect to time. Substituting Eq. (1) in Eq. (3), considering a transversely isotropic elastic solid, if the z axis is normal to the plane of isotropy, and for a two-dimensional problem, $\partial/\partial x_3 = 0$, one can write:

$$\rho \ddot{u}_1 = \left(c_{11}u_{1,1} + c_{12}u_{2,2}\right)_{,1} + \left[c_{66}\left(u_{1,2} + u_{2,1}\right)\right]_{,2},$$

$$\rho \ddot{u}_2 = \left(c_{12}u_{1,1} + c_{11}u_{2,2}\right)_{,2} + \left[c_{66}\left(u_{1,2} + u_{2,1}\right)\right]_{,1},$$

$$\rho \ddot{u}_3 = \left(c_{44}u_{3,1} + e_{15}\phi_{,1} + q_{15}\varphi_{,1}\right)_{,1} + \left(c_{44}u_{3,2} + e_{15}\phi_{,2} + q_{15}\varphi_{,2}\right)_{,2},$$

$$0\ddot{\phi} = \left(e_{15}u_{3,1} - \epsilon_{11}\phi_{,1} - \lambda_{11}\varphi_{,1}\right)_{,1} + \left(e_{15}u_{3,2} - \epsilon_{11}\phi_{,2} - \lambda_{11}\varphi_{,2}\right)_{,2},$$

$$0\ddot{\varphi} = \left(q_{15}u_{3,1} - \lambda_{11}\phi_{,1} - \Gamma_{11}\varphi_{,1}\right)_{,1} + \left(q_{15}u_{3,2} - \lambda_{11}\phi_{,2} - \Gamma_{11}\varphi_{,2}\right)_{,2}, \tag{4}$$

or in a vectorial notation:

$$\rho\ddot{u}_i = \boldsymbol{\nabla}_T \cdot (c_{66}\boldsymbol{\nabla}_T u_i) + \boldsymbol{\nabla}_T \cdot \left(c_{66}\frac{\partial \mathbf{u}_T}{\partial x_i}\right) + \frac{\partial}{\partial x_i}[(c_{11} - 2c_{66})\boldsymbol{\nabla}_T \cdot \mathbf{u}_T], \qquad (i,j = 1,2),$$

$$\rho\ddot{u}_3 = \boldsymbol{\nabla}_T \cdot (c_{44}\boldsymbol{\nabla}_T u_3 + e_{15}\boldsymbol{\nabla}_T\phi + q_{15}\boldsymbol{\nabla}_T\varphi),$$

$$0\ddot{\phi} = \boldsymbol{\nabla}_T \cdot (e_{15}\boldsymbol{\nabla}_T u_3 - \epsilon_{11}\boldsymbol{\nabla}_T\phi - \lambda_{11}\boldsymbol{\nabla}_T\varphi),$$

$$0\ddot{\varphi} = \boldsymbol{\nabla}_T \cdot (q_{15}\boldsymbol{\nabla}_T u_3 - \lambda_{11}\boldsymbol{\nabla}_T\phi - \Gamma_{11}\boldsymbol{\nabla}_T\varphi), \tag{5}$$

where $c_{66} = \frac{1}{2}(c_{11} - c_{12})$, $\boldsymbol{\nabla}_T = (\partial/\partial x_1)\mathbf{e}_1 + (\partial/\partial x_2)\mathbf{e}_2$, $\mathbf{u}_T = u_1\mathbf{e}_1 + u_2\mathbf{e}_2$ and $\mathbf{e}_\mathrm{i}$ $(i = 1,2)$ are the basis vectors in the real space.

Besides, considering a MPC one can note that $c_{11} = c_{11}(\mathbf{r})$, $c_{12} = c_{12}(\mathbf{r})$, $c_{66} = c_{66}(\mathbf{r})$, $c_{44} = c_{44}(\mathbf{r})$, $e_{15} = e_{15}(\mathbf{r})$, $q_{15} = q_{15}(\mathbf{r})$, $\epsilon_{11} = \epsilon_{11}(\mathbf{r})$, $\lambda_{11} = \lambda_{11}(\mathbf{r})$, $\Gamma_{11} = \Gamma_{11}(\mathbf{r})$, $\rho = \rho(\mathbf{r})$, $u_i = u_i(\mathbf{r},t)$, $\phi = \phi(\mathbf{r},t)$, $\varphi = \varphi(\mathbf{r},t)$. For a two-dimensional periodicity (the system has translational symmetry in *z* direction and the material parameters depend only on the *x* and *y* coordinates), then $\mathbf{r} = x\mathbf{e}_1 + y\mathbf{e}_2$ is the two-dimensional spatial vector.

In order to eliminate the factor time in Eq. (4) and Eq. (5), we imposed a harmonic time dependence on $u_i(\mathbf{r},t) = u_i(\mathbf{r})e^{i\omega t}$, $\phi(\mathbf{r},t) = \phi(\mathbf{r})e^{i\omega t}$ and $\varphi(\mathbf{r},t) = \varphi(\mathbf{r})e^{i\omega t}$, where ω is the angular frequency. Applying the Floquet-Bloch's theorem (Floquet, 1883; Bloch, 1928), expanding u_i, ϕ and φ as a Fourier series and considering wave propagation in the *xy* plane ($K_3 = 0$), one can write:

$$T(\mathbf{r}) = e^{i\mathbf{K}.\mathbf{r}}T_\mathbf{K}(\mathbf{r}) = e^{i\mathbf{K}.\mathbf{r}}\sum_{\mathbf{G}=-\infty}^{+\infty} T(\mathbf{G})\, e^{i\mathbf{G}.\mathbf{r}} = \sum_{\mathbf{G}=-\infty}^{+\infty} T(\mathbf{G})\, e^{i(\mathbf{K}+\mathbf{G}).\mathbf{r}}, \tag{6}$$

where $T(\mathbf{r})$ can be $u_i(\mathbf{r})$, $\phi(\mathbf{r})$ or $\varphi(\mathbf{r})$, $T_\mathbf{K}(\mathbf{r})$ is the amplitude of the Bloch wave, note that $T_\mathbf{K}(\mathbf{r}) = T_\mathbf{K}(\mathbf{r}+\mathbf{R})$ and $T(\mathbf{r}+\mathbf{R}) = T(\mathbf{r})e^{i\mathbf{K}.\mathbf{R}}$, $e^{i\mathbf{K}.\mathbf{R}}$ is called the Bloch periodic boundary condition, $\mathbf{K} = u\mathbf{b}_1 + v\mathbf{b}_2$ is the Bloch wave vector, $u,v \in \mathbb{Q}$ are the symmetry points within the IBZ in reciprocal space, or one may write $\mathbf{K} = k_1\mathbf{e}_1 + k_2\mathbf{e}_2$, $k_1, k_2 \in \mathbb{R}$ are the point coordinates within the IBZ in Figure 1 (d), (e) and (f) for the reciprocal space, $\mathbf{b}_\mathrm{i}$ $(i = 1,2)$ are the basis vectors in the reciprocal space defined as $\mathbf{a}_\mathrm{i} \cdot \mathbf{b}_\mathrm{j} = 2\pi\delta_{ij}$, $\mathbf{b}_1 = 2\pi\frac{\mathbf{a}_2\times\mathbf{a}_3}{\mathbf{a}_1\cdot(\mathbf{a}_2\times\mathbf{a}_3)}$, $\mathbf{b}_2 = 2\pi\frac{\mathbf{a}_3\times\mathbf{a}_1}{\mathbf{a}_2\cdot(\mathbf{a}_3\times\mathbf{a}_1)}$, $\mathbf{a}_\mathrm{i}$ $(i = 1,2)$ are the components of the lattice vector $\mathbf{R} = (\bar{m}\mathbf{a}_1 + \bar{n}\mathbf{a}_2)$, $\bar{m},\bar{n} \in \mathbb{Z}$.

For a square lattice $\mathbf{a}_\mathrm{i} = a\mathbf{e}_\mathrm{i}$ $(i = 1,2)$, for triangular lattice $\mathbf{a}_1 = a\mathbf{e}_1$, $\mathbf{a}_2 = \frac{a}{2}\mathbf{e}_1 + \frac{a\sqrt{3}}{2}\mathbf{e}_2$, for a honeycomb lattice $\mathbf{a}_1 = \frac{a\sqrt{3}}{2}\mathbf{e}_1 + \frac{3a}{2}\mathbf{e}_2$, $\mathbf{a}_2 = -\frac{a\sqrt{3}}{2}\mathbf{e}_1 + \frac{3a}{2}\mathbf{e}_2$ and a is the lattice parameter. For square lattice, the reciprocal lattice vector is defined as $\mathbf{G} = \frac{2\pi}{a}(m\mathbf{e}_1 + n\mathbf{e}_2)$, for triangular lattice $\mathbf{G} = \frac{2\pi}{a}\left[m\mathbf{e}_1 + \frac{(-m+2n)}{\sqrt{3}}\mathbf{e}_2\right]$ and for honeycomb lattice $\mathbf{G} = \frac{2\pi}{a\sqrt{3}}\left[(m-n)\mathbf{e}_1 + \frac{(m+n)}{\sqrt{3}}\mathbf{e}_2\right]$, $m,n \in \mathbb{Z}$. Note that $\mathbf{G}$ is a two-dimensional vector because we consider a two-dimensional periodicity.

Furthermore, one may write:

$$P(\mathbf{r}) = \sum_{\mathbf{G}'=-\infty}^{+\infty} P(\mathbf{G}')\, e^{i\mathbf{G}'.\mathbf{r}}, \tag{7}$$

where P is one of the $c_{11}, c_{12}, c_{66}, c_{44}, e_{15}, q_{15}, \epsilon_{11}, \lambda_{11}, \Gamma_{11}, \rho$ and $\mathbf{G}'$ has the same expressions of $\mathbf{G}$ with m', $n' \in \mathbb{Z}$. Note that we use $\mathbf{G}'$ to highlight the difference between the expansions of material properties and the displacements and potentials.

Substituting Eqs. (6) and (7) in Eq. (4) or Eq. (5), with $\mathbf{G}'' = \mathbf{G}' + \mathbf{G}$, multiplying by $e^{-i\mathbf{G}'.\mathbf{r}}$ and integrating over the unit cell, one may write:

$$\sum_{\mathbf{G}} \left(\omega^2 \begin{bmatrix} \rho(\mathbf{G}'-\mathbf{G}) & \mathbf{0} & \mathbf{0} & \mathbf{0} & \mathbf{0} \\ \mathbf{0} & \rho(\mathbf{G}'-\mathbf{G}) & \mathbf{0} & \mathbf{0} & \mathbf{0} \\ \mathbf{0} & \mathbf{0} & \rho(\mathbf{G}'-\mathbf{G}) & \mathbf{0} & \mathbf{0} \\ \mathbf{0} & \mathbf{0} & \mathbf{0} & \mathbf{0} & \mathbf{0} \\ \mathbf{0} & \mathbf{0} & \mathbf{0} & \mathbf{0} & \mathbf{0} \end{bmatrix} \right) \begin{Bmatrix} \mathrm{u}_1(\mathbf{G}) \\ \mathrm{u}_2(\mathbf{G}) \\ \mathrm{u}_3(\mathbf{G}) \\ \phi(\mathbf{G}) \\ \varphi(\mathbf{G}) \end{Bmatrix}$$
$$= \sum_{\mathbf{G}} \begin{bmatrix} \mathbf{Q}_{11} & \mathbf{Q}_{12} & \mathbf{0} & \mathbf{0} & \mathbf{0} \\ \mathbf{Q}_{21} & \mathbf{Q}_{22} & \mathbf{0} & \mathbf{0} & \mathbf{0} \\ \mathbf{0} & \mathbf{0} & \mathbf{Q}_{33} & \mathbf{Q}_{34} & \mathbf{Q}_{35} \\ \mathbf{0} & \mathbf{0} & \mathbf{Q}_{43} & \mathbf{Q}_{44} & \mathbf{Q}_{45} \\ \mathbf{0} & \mathbf{0} & \mathbf{Q}_{53} & \mathbf{Q}_{54} & \mathbf{Q}_{55} \end{bmatrix} \begin{Bmatrix} \mathrm{u}_1(\mathbf{G}) \\ \mathrm{u}_2(\mathbf{G}) \\ \mathrm{u}_3(\mathbf{G}) \\ \phi(\mathbf{G}) \\ \varphi(\mathbf{G}) \end{Bmatrix}, \tag{8}$$

where

$$\mathbf{Q}_{11} = c_{11}(\mathbf{G}'-\mathbf{G})(\mathbf{K}+\mathbf{G})_1(\mathbf{K}+\mathbf{G}')_1 + c_{66}(\mathbf{G}'-\mathbf{G})(\mathbf{K}+\mathbf{G})_2(\mathbf{K}+\mathbf{G}')_2,$$
$$\mathbf{Q}_{12} = c_{12}(\mathbf{G}'-\mathbf{G})(\mathbf{K}+\mathbf{G})_2(\mathbf{K}+\mathbf{G}')_1 + c_{66}(\mathbf{G}'-\mathbf{G})(\mathbf{K}+\mathbf{G})_1(\mathbf{K}+\mathbf{G}')_2,$$
$$\mathbf{Q}_{21} = c_{12}(\mathbf{G}'-\mathbf{G})(\mathbf{K}+\mathbf{G})_1(\mathbf{K}+\mathbf{G}')_2 + c_{66}(\mathbf{G}'-\mathbf{G})(\mathbf{K}+\mathbf{G})_2(\mathbf{K}+\mathbf{G}')_1,$$
$$\mathbf{Q}_{22} = c_{11}(\mathbf{G}'-\mathbf{G})(\mathbf{K}+\mathbf{G})_2(\mathbf{K}+\mathbf{G}')_2 + c_{66}(\mathbf{G}'-\mathbf{G})(\mathbf{K}+\mathbf{G})_1(\mathbf{K}+\mathbf{G}')_1,$$
$$\mathbf{Q}_{33} = c_{44}(\mathbf{G}'-\mathbf{G})(\mathbf{K}+\mathbf{G})_1(\mathbf{K}+\mathbf{G}')_1 + c_{44}(\mathbf{G}'-\mathbf{G})(\mathbf{K}+\mathbf{G})_2(\mathbf{K}+\mathbf{G}')_2,$$
$$\mathbf{Q}_{34} = e_{15}(\mathbf{G}'-\mathbf{G})(\mathbf{K}+\mathbf{G})_1(\mathbf{K}+\mathbf{G}')_1 + e_{15}(\mathbf{G}'-\mathbf{G})(\mathbf{K}+\mathbf{G})_2(\mathbf{K}+\mathbf{G}')_2,$$
$$\mathbf{Q}_{35} = q_{15}(\mathbf{G}'-\mathbf{G})(\mathbf{K}+\mathbf{G})_1(\mathbf{K}+\mathbf{G}')_1 + q_{15}(\mathbf{G}'-\mathbf{G})(\mathbf{K}+\mathbf{G})_2(\mathbf{K}+\mathbf{G}')_2,$$
$$\mathbf{Q}_{43} = \mathbf{Q}_{34},$$
$$\mathbf{Q}_{44} = -\epsilon_{11}(\mathbf{G}'-\mathbf{G})(\mathbf{K}+\mathbf{G})_1(\mathbf{K}+\mathbf{G}')_1 - \epsilon_{11}(\mathbf{G}'-\mathbf{G})(\mathbf{K}+\mathbf{G})_2(\mathbf{K}+\mathbf{G}')_2,$$
$$\mathbf{Q}_{45} = -\lambda_{11}(\mathbf{G}'-\mathbf{G})(\mathbf{K}+\mathbf{G})_1(\mathbf{K}+\mathbf{G}')_1 - \lambda_{11}(\mathbf{G}'-\mathbf{G})(\mathbf{K}+\mathbf{G})_2(\mathbf{K}+\mathbf{G}')_2,$$
$$\mathbf{Q}_{53} = \mathbf{Q}_{35},$$
$$\mathbf{Q}_{54} = \mathbf{Q}_{45},$$
$$\mathbf{Q}_{55} = -\Gamma_{11}(\mathbf{G}'-\mathbf{G})(\mathbf{K}+\mathbf{G})_1(\mathbf{K}+\mathbf{G}')_1 - \Gamma_{11}(\mathbf{G}'-\mathbf{G})(\mathbf{K}+\mathbf{G})_2(\mathbf{K}+\mathbf{G}')_2, \tag{9}$$

where K_1, K_2, G_1 G_2, G_1' and G_2' are the *x* and *y* components of $\mathbf{K}$, $\mathbf{G}$ and $\mathbf{G}'$, respectively.

Equation (8) represents a generalized eigenvalue problem of $\omega^2(\mathbf{K})$ and should be solved for each $\mathbf{K}$ into the IBZ for square, Fig. 1 (d), triangular, Fig. 1 (e) and honeycomb lattices, Fig. 1 (f).

The Fourier coefficients are:

$$P(\mathbf{G}) = \begin{cases} fP_{\mathrm{A}} + (1-f)P_{\mathrm{B}} \text{ for } \mathbf{G} = \mathbf{0} \\ (P_{\mathrm{A}} - P_{\mathrm{B}})F(\mathbf{G}) \text{ for } \mathbf{G} \neq \mathbf{0} \end{cases}, \tag{10}$$

where the indexes *A* and *B* of Eq. (10) are related to the inclusion ($BaTiO_3$–$CoFe_2O_4$) and the matrix (polymer), respectively, $F(\mathbf{G})$ is the structure function and f is the filling fraction of each type of inclusion, *i.e.* circular section of radius r', square section of width $2l$, rotated square section of width $2l$ with a 45° angle of rotation with respect to x and y axes and a hollow circular section with external radius R' and internal radius r, $R' > r'$. The hollow cylinder has an internal radius r' of polymer and a thickness $R' - r'$ of $BaTiO_3$–$CoFe_2O_4$. The filling fraction $f = S_A/S_c$, where S_A is the cross section area of the inclusion and $S_c = \|\mathbf{a}_1 \times \mathbf{a}_2\|$ is the cross section area of the unit cell and for square lattice is:

$$f = \begin{cases} \pi r'^2/a^2 \text{ for circular section} \\ 4l^2/a^2 \text{ for square section} \\ 4l^2/a^2 \text{ for square rotated section} \\ \pi(R'^2 - r'^2)/a^2 \text{ for hollow section} \end{cases}. \tag{11}$$

The filling fraction f for triangular lattice is:

$$f = \begin{cases} 2\pi r'^2/\sqrt{3}a^2 \text{ for circular section} \\ 8l^2/\sqrt{3}a^2 \text{ for square section} \\ 8l^2/\sqrt{3}a^2 \text{ for square rotated section} \\ 2\pi(R'^2 - r'^2)/\sqrt{3}a^2 \text{ for hollow section} \end{cases}, \tag{12}$$

and for honeycomb lattice is:

$$f = \begin{cases} 4\pi r'^2/3\sqrt{3}a^2 \text{ for circular section} \\ 16l^2/3\sqrt{3}a^2 \text{ for square section} \\ 16l^2/3\sqrt{3}a^2 \text{ for square rotated section} \\ 4\pi(R'^2 - r'^2)/3\sqrt{3}a^2 \text{ for hollow section} \end{cases}. \tag{13}$$

The structure function $F(\mathbf{G})$ for square and triangular lattices is defined as:

$$F(\mathbf{G}) = \frac{1}{S_A}\iint e^{-i\mathbf{G}\cdot\mathbf{r}}\, d^2r. \tag{14}$$

The integral in Eq. (14) is performed over the cross section of the $BaTiO_3$–$CoFe_2O_4$ inclusion. The structure functions of the inclusions for square and triangular lattices are:

$$F(\mathbf{G}) = \begin{cases} 2fJ_1(Gr')/Gr' \text{ for circular section} \\ f[\sin(G_1r')/G_1r][\sin(G_2r')/G_2r'] \text{ for square section} \\ f\left\{\dfrac{\sin\left[(l/\sqrt{2})(G_1+G_2)\right]}{(l/\sqrt{2})(G_1+G_2)}\right\}\left\{\dfrac{\sin\left[(l/\sqrt{2})(-G_1+G_2)\right]}{(l/\sqrt{2})(-G_1+G_2)}\right\} \text{ for square rotated section} \\ 2f[J_1(GR') - (r'/R')J_1(GR')]/(GR') \text{ for hollow section} \end{cases}, \tag{15}$$

where $G = \|\mathbf{G}\|$.

The structure function $F(\mathbf{G})$ for honeycomb lattice is defined as (Cassagne *et al.*, 1996):

$$F(\mathbf{G}) = 2\cos(\mathbf{G}\cdot\mathbf{u}_1')\frac{1}{S_B}\iint e^{-i\mathbf{G}\cdot\mathbf{r}}\, d^2r, \tag{16}$$

where $\mathbf{u}_1' = -\mathbf{u}_2' = a(0,1/2)$ are the vectors that define the central position of the two scatterers into the honeycomb unit cell. We chose these vectors similar as Gao *et al.* (2013).

Thus, the structure functions of the inclusions for honeycomb lattice are the same of Eq. (15) multiplied by $\cos(\mathbf{G}\cdot\mathbf{u}_1')$, considering f from Eq. (13), or the same of Eq. (15) multiplied by $2\cos(\mathbf{G}\cdot\mathbf{u}_1')$, considering $f = f/2$ from Eq. (13), because we defined for honeycomb lattice $f = 2S_A/S_c$.

3 RESULTS AND DISCUSSION

The physical parameters of $BaTiO_3$–$CoFe_2O_4$ (A) and the polymer (B) are listened in Table 1.

Table 1. Physical parameters of $BaTiO_3$–$CoFe_2O_4$ (material A) and polymer (material B) (Wang *et al.*, 2009).

	ρ	c_{11}	c_{12}	c_{44}	c_{66}	e_{15}	ϵ_{11}	q_{15}	Γ_{11}	λ_{11}
A	5.73	166	77	43	44.5	11.6	11.2	550	5	0.005
B	1.15	7.8	4.7	4.6	1.55	0	0.0398	0	5	0

ρ in 10^3 kg/m^3, c_{ij} in 10^9 N/m^2, e_{15} in C/m^2, ϵ_{11} in 10^{-9} C^2/Nm^2, q_{15} in N/Am, Γ_{11} in Ns^2/C^2, λ_{11} in 10^{-9} Ns/VC.

We calculated the band structure considering a fixed filling fraction (0.45) and a lattice parameter (0.022 m) for the four inclusions considering square, triangular and honeycomb lattices. In the course of the numerical calculations, the integers $m,\ n,\ m',\ n'$ were limited to the interval $[-10, 10]$ for all results, *i.e.* 441 plane waves. This resulted in a very good convergence. One can note that we restricted the band structure plots comparison until a maximum frequency (150 kHz) instead of fixing the number of bands.

The Fig. 2 (a-d) compares the band structure of a square lattice illustrated in Fig. 1 (a) and (d) for the four types of inclusions, considering the *XY* (red) and *Z* (blue) modes. Note from Eqs. (4), (5) or (8) that only the *Z* mode contains the piezoelectric and piezomagnetic effects. We plot the band structure in the three principal symmetry directions of the IBZ (Fig. 1 (d)). The plots are given in terms of frequency in Hz versus the reduced Bloch wave vector $\mathbf{k} = \mathbf{K}a/2\pi$. In Fig. 2 (a), three complete band gaps are found for circular cross section inclusion.

The relation between the parameters R' and r' for hollow circular cross section inclusion was fixed in $r' = 0.2R'$ and we did not investigate the influence of the thickness $R' - r'$ of $BaTiO_3$–$CoFe_2O_4$ in the band structure. Figure 2 (b) presents one complete band gap and one can observe that the first bands occur in higher frequencies compared to the other inclusions. Figure 2 (c) shows two complete band gaps for square cross section inclusion and its first band gap is the broader one for a square lattice.

When these square inclusions are rotated 45° with respect to *x* and *y* axes, another gap was created in higher frequencies and one narrow gap was created around 50 kHz, as illustrated in Figure 2 (d). The square inclusion presented the best performance (broader band gap) in lower frequencies compared to the other inclusions for square lattice. However, the circular and rotated square inclusions presented more band gaps.

Figure 3 shows the band structures for a triangular lattice illustrated in Fig. 1 (b) and (e) considering *XY* and *Z* modes. For circular, square and rotated square inclusions, Fig. 3 (a), (c) and (d), respectively, presents a complete wide band gap between the *XY* and *Z* mode bands in, approximately, the same range of frequency, *i.e.* 40–75 kHz. For hollow

inclusion, with the same thickness as cited above, only one wide gap was created between 73–100 kHz.

In Figure 4, for honeycomb lattice as illustrated in Fig. 1 (c) and (f), the band structures of square and rotated square inclusions presented almost the same gaps. The band structure of circular inclusion creates four gaps, however, all of them narrower than the gaps of square and triangular lattices. For hollow inclusion, one can observe one complete band gap and the first bands occur in higher frequencies compared to the other inclusions, similar to square and triangular lattices.

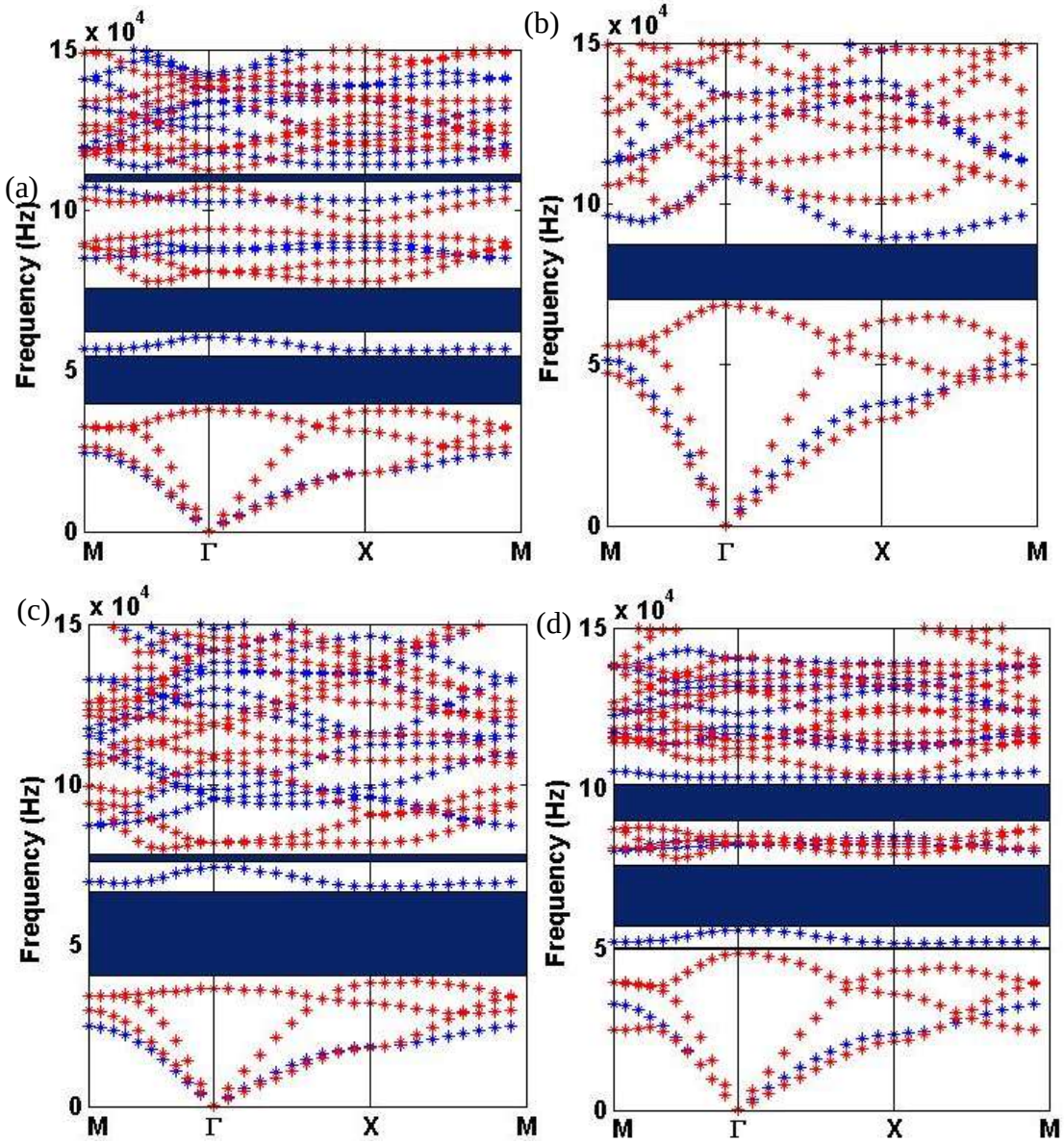

Figure 2. Elastic band structures of XY (red) and Z (blue) modes of $BaTiO_3$–$CoFe_2O_4$ inclusions in a polymer matrix for a square lattice. The following types of inclusions are considered: (a) circular, (b) hollow circular, (c) square and (d) rotated square with a 45° angle of rotation with respect to the *x*, *y* axes.

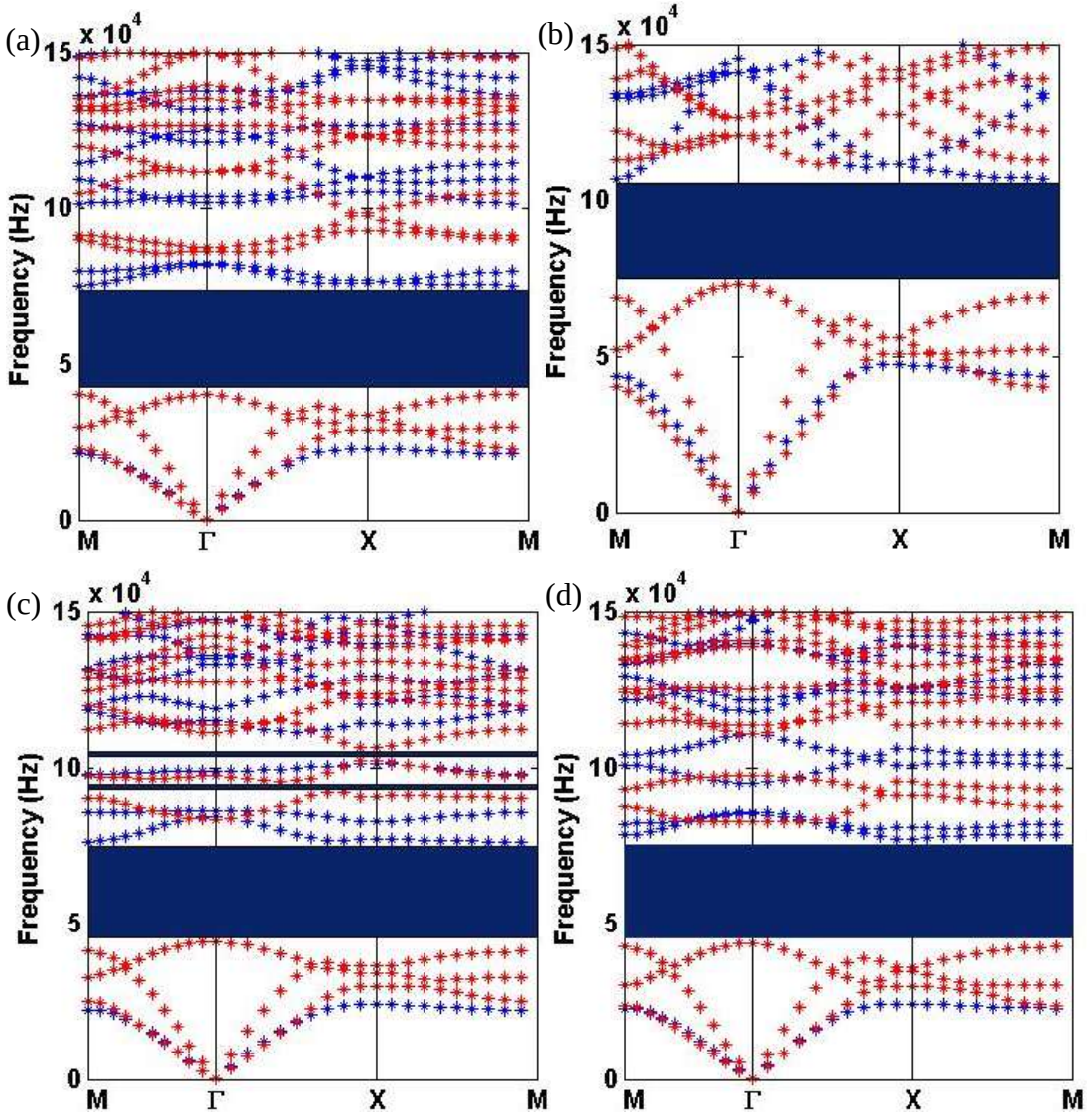

Figure 3. Elastic band structures of XY (red) and Z (blue) modes of $BaTiO_3$–$CoFe_2O_4$ inclusions in a polymer matrix for a triangular lattice. The following types of inclusions are considered: (a) circular, (b) hollow circular, (c) square and (d) rotated square with a 45° angle of rotation with respect to the *x, y* axes.

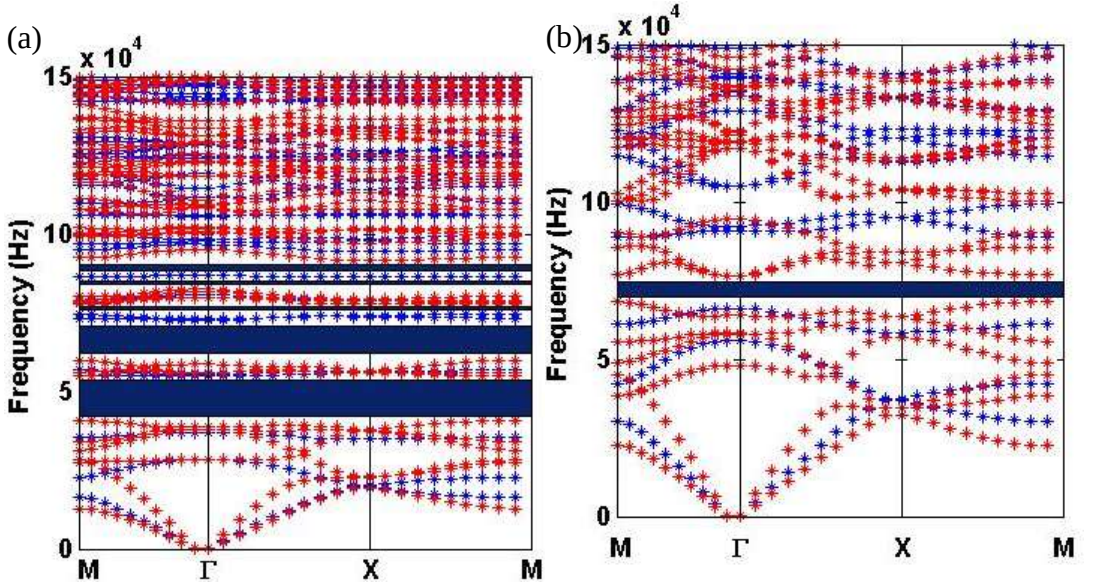

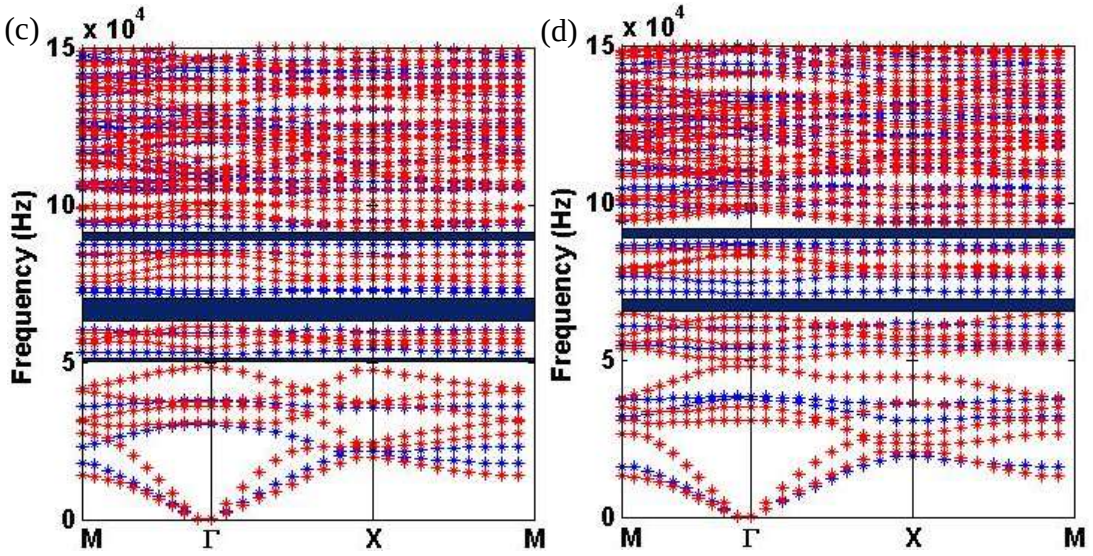

Figure 4. Elastic band structures of XY (red) and Z (blue) modes of $BaTiO_3$–$CoFe_2O_4$ inclusions in a polymer matrix for a honeycomb lattice. The following types of inclusions are considered: (a) circular, (b) hollow circular, (c) square and (d) rotated square with a 45° angle of rotation with respect to the *x, y* axes.

4 CONCLUSIONS

We obtained relatively broad complete band gaps between *XY* and *Z* modes where the propagation of elastic waves is forbidden. In the case of triangular array of $BaTiO_3$–$CoFe_2O_4$ inclusions embedded in a polymer background, the band structures considering circular, square and rotated square with a 45° angle of rotation with respect to the *x, y* axes inclusions presented approximately the similar behavior and the complete band gap arise in almost the same range of frequency. The band structure considering hollow circular inclusion presented one complete band gap between 73–100 kHz for $r' = 0.2R'$. Unlike triangular lattice, for the square lattice, different behaviors of the band structure have been obtained for all inclusions. The best performance in lower frequencies was found for square inclusion.

For honeycomb lattice, the band structures of square and rotated square inclusions present almost the same gaps, however, all of them narrower than the gaps of square and triangular lattices. For hollow inclusion, only one complete band gap was created. The best performance for honeycomb lattice was considering the circular inclusion.

We considered square, triangular and honeycomb arrays of inclusions perfectly embedded in an elastic background. This means that we neglected the effects due to decohesion of the fibers from the polymer matrix and to roughness at the interface between the inclusions and the matrix. These defects could modify the elastic wave propagation in composite materials, altering the band structure of them. The elastic band gaps in MPC enlarge the potential applications for vibration management.

ACKNOWLEDGEMENTS

The authors gratefully acknowledge the Brazilian research funding agency FAPEMA and IFMA for their financial support of this investigation.

REFERENCES

Anjos, V. & Arantes, A., 2015. Phononic band structure in carbon microtube composites. *RSC Advances*, Vol. 5, pp. 11248–11253.

Benchabane, S., Khelif, A., Robert, L., Rauch, J.Y., Pastureaud, T. & Laude, V. 2006. Elastic band gaps for surface modes in an ultrasonic lithium niobate phononic crystal, *Proceedings SPIE*, vol. 6182, n. 618216, pp. 1–13.

Bloch, F., 1928. Über die Quantenmechanik der Electron in Kristallgittern. *Zeitschrift für Physik*, vol. 52, pp. 550–600.

Bou Matar, O., Robillard, J.F., Vasseur, J.O., Hladky-Hennion, A.-C. & Deymier P.A., 2012. Band gap tunability of magneto-elastic phononic crystal. *Journal of Applied Physics*, vol. 111, n. 054901, pp. 1–15.

Casadei, F., Dozio, L., Ruzzene, M. & Cunefare, K.A., 2010. Periodic shunts arrays for the control of noise radiation in an enclosure. *Journal of Sound and Vibration*, vol. 329, pp. 3632–3646.

Casadei, F., Beck, B.S., Cunefare, K.A. & Ruzzene, M., 2012. Vibration control of plates through hybrid configurations of periodic piezoeletric shunts. *Journal of Intelligent Material Systems and Structures*, vol. 23, n. 10, pp. 1169–1177.

Cassagne, D., Jouanin, C., Bertho, D., 1996. Hexagonal photonic-band gap structures. *Physical Review B*, vol. 53, n. 11, pp. 7134–7142.

Dyogtyev, A.V., Sukhoivanov, I.A., De La Rue, R.M., 2010. Photonic band-gaps maps for different two dimensionally periodic photonic crystal structures. *Journal of Applied Physics*, vol. 107, n. 013108, pp. 1–7.

Floquet, G., 1883. Sur les équations différentielles linéaires à coefficients périodiques. *Annales scientifiques de l'École Normale Supérieure*, vol. 12, pp. 47–88.

Gao, Z., Fang, J., Zhang, Y., Jiang, L., 2013. Band structure research of a 2D honeycomb lattice phononic crystal. *International Journal of Electrochemical Science*, vol. 8, pp. 7918–7925.

Ho, K.M., Cheng, C.K., Yang, Z., Zhang, X.X. & Sheng, P., 2003. Broadband locally resonant sonic shields. *Applied Physics Letters*, vol. 83, n. 26, pp. 5566–5568.

Hou, Z., Wu, F. & Liu, Y., 2004. Phononic crystals containing piezoelectric material. . *Solid State Communications*, vol. 130, pp. 745–749.

Huang, J. & Shi, Z., 2013. Attenuation zones of periodic pile barriers and its application in vibration reduction for plane waves. *Journal of Sound and Vibration*, vol. 332, pp. 4423–4439.

Jensen, J.S., 2003. Phononic band gaps and vibrations in one- and two-dimensional mass-spring structures. *Journal of Sound and Vibration*, vol. 266, pp. 1053–1078.

Kushwaha, M.S., Halevi, P. & Martínez, G., 1994, Theory of acoustic band structure of periodic elastic composites, *Physical Review B*, vol. 49, pp. 2313–2322.

Lian, Z., Jiang, S., Hu, H., Dai, L., Chen, X. & Jiang, W., 2016. An enhanced plane wave expansion method to solve piezoelectric phononic crystal with resonant shunting circuits. *Shock and Vibration*, vol. 2016, n. 4015363, pp. 1–13.

Miranda Jr., E.J.P. & Dos Santos, J.M.C., 2015. Flexural wave band gaps in metamaterial elastic beam, *Proceedings of the 23rd ABCM International Congress of Mechanical Engineering*, Rio de Janeiro, Brazil, pp. 1–8.

Miranda Jr., E.J.P. & Dos Santos, J.M.C., 2016a. Phononic band gaps in Al_2O_3/epoxy composite, *Submitted to Materials Science Forum*, pp. 1–10.

Miranda Jr., E.J.P. & Dos Santos, J.M.C., 2016b. Flexural wave band gaps in elastic metamaterial thin plate, *Proceedings of the IX Mechanical Engineering Brazilian Congress*, Fortaleza, Brazil, pp. 1–10.

Miranda Jr., E.J.P. & Dos Santos, J.M.C., 2016c. Flexural wave band gaps in Al_2O_3/epoxy composite rectangular plate using Mindlin theory, *Proceedings of the 3rd Brazilian Conference on Composite Materials*, Gramado, Brazil, pp. 1–8.

Olsson III, R.H. & El-Kady, I., 2009. Microfabricated phononic crystal devices and applications, *Measurement Science and Technology*, vol. 20, n. 012002, pp. 1–13.

Pennec, Y., Vasseur, J.O., Djafari-Rouhani, B., Dobrzyński, L. & Deymier, P.A., 2010. Two-dimensional phononic crystals: Examples and applications. *Surface Science Reports*, vol. 65, pp. 229–291.

Qiu, C.Y., Liu, Z.Y., Mei, J. & Shi, J., 2005. Mode-selecting acoustic filter by using resonant tunneling of two-dimensional double phononic crystals, *Applied Physics Letters*, vol. 87, n. 104101, pp. 1–3.

Robillard, J.-F., Bou Matar, O., J.F., Vasseur, J.O., Deymier P.A., Stippinger, M., Hladky-Hennion, A.-C, Pennec, Y. & Djafari-Rouhani, B., 2009. Tunable magnetoelastic phononic crystals. *Applied Physics Letters*, vol. 95, n. 124104, pp. 1–4.

Sigalas, M.M. & Economou, E.N., 1994. Elastic waves in plates with periodically placed inclusions. *Journal of Applied Physics*, vol. 75, pp. 2845–2850.

Vasseur, J.O., Bou Matar, O., J.F., Robillard, J.-F., Hladky-Hennion, A.-C & Deymier P.A., 2011. Band structures tunability of bulk 2D phononic crystals made of magneto-elastic materials. *AIP Advances*, vol. 1, n. 041904, pp. 1–13.

Wang, G., Wen, J.H. & Wen, X.S., 2005. Quasi-one-dimensional phononic crystals studied using the improved lumped-mass method: application to locally resonant beams with flexural wave band gap, *Physical Review B*, vol. 71, n. 104302, pp. 1–5.

Wang, X.-M. & Shen, Y.-P., 1996. The conservations laws and path-independent integrals with an application for linear electro-magneto-elastic media, *International Journal of Solids and Structures*, vol. 33, n. 6, pp. 865–878.

Wang, Y.-Z., Li, F.-M., Huang, W.-H., Jiang, X., Wang, Y.-S. & Kishimoto, K., 2008. Wave band gaps in two-dimensional piezoelectric/piezomagnetic phononic crystals, *International Journal of Solids and Structures*, vol. 48, pp. 4203–4210.

Wang, Y.-Z., Li, F.-M., Kishimoto, K., Wang, Y.-S. & Huang, W.-H., 2009. Elastic wave band gaps in magnetoelectroelastic phononic crystals, *Wave Motion*, vol. 46, pp. 47–56.

Wilm, M., Ballandras, S., Laude, V. & Pastureaud, T., 2001. A plane-wave-expansion approach for modelling acoustic propagation in 2D and 3D piezoelectric periodic structures. *IEEE Ultrasonics Symposium*, vol. 2, pp. 977–980.

Wilm, M., Ballandras, S., Laude, V. & Pastureaud, T., 2002. A full 3D plane-wave-expansion model for 1-3 piezoelectric composite structures. *Journal of the Acoustical Society of America,* vol. 112, n. 3, pp. 943–952.

Wilm, M., Khelif, A., Ballandras, S. & Laude, V., 2003. Out-of-plane propagation of elastic waves in two-dimensional phononic band-gap materials. *Physical Review E*, vol. 67, n. 065602, pp. 1–4.

Xiao, Y., Wen, J. & Wen, X., 2012. Sound transmission loss of metamaterial-based thin plates with multiple subwavelength arrays of attached resonators. *Journal of Sound and Vibration,* vol. 331, pp. 5408–5423.

Yang, Z., Dai, H.M., Chan, N.H. & Ma, G.C., 2003. Acoustic metamaterial panels for sound attenuation in the 50–1000 Hz regime. *Applied Physics Letters*, vol. 96, n. 041906, pp. 1–3.

Yu, K., Chen, T. & Wang, X., 2013. Band gaps in the low-frequency range based on the two-dimensional phononic crystals plates composed of rubber matrix with periodic steel stubs. *Physica B*, vol. 416, pp. 12–16.